Computerized Medical Imaging and Graphics 33 (2009) 187–196

Contents lists available at ScienceDirect

Computerized Medical Imaging and Graphics

journal homepage: www.elsevier.com/locate/compmedimag

Contrast enhancement and tissues classification of breast MRI using Kalman filter-based linear mixing method

Sheng-Chih Yang[a], Chuin-Mu Wang[a], Hsian-He Hsu[b], Pau-Choo Chung[c,*], Giu-Cheng Hsu[b], Chun-Jung Juan[b], Chien-Shun Lo[d]

[a] Department of Computer Science and Information Engineering, National Chin Yi University of Technology, Taichung 411, Taiwan, ROC
[b] Department of Radiology, Tri-Service General Hospital and National Defense Medical Center, Taipei 114, Taiwan, ROC
[c] Department of Electrical Engineering, Institute of Computer and Communication Engineering, National Cheng Kung University, No. 1 University Road, Tainan 701, Taiwan, ROC
[d] Department of Multimedia Design, National Formosa University, Yun-Lin 632, Taiwan, ROC

ARTICLE INFO

Article history:
Received 20 May 2008
Received in revised form
10 November 2008
Accepted 1 December 2008

Keywords:
Contrast enhancement
Breast MRI
Breast cancer screening
Kalman filter
Linear spectral mixture model
Tissue classification

ABSTRACT

Much attention is currently focused on one of the newest breast examination techniques, breast MRI. Contrast-enhanced breast MRIs acquired by contrast injection have been shown to be very sensitive in the detection of breast cancer, but are also time-consuming and cause waste of medical resources. This paper therefore proposes the use of spectral signature detection technology, the Kalman filter-based linear mixing method (KFLM), which can successfully present the results as high-contrast images and classify breast MRIs into major tissues from four bands of breast MRIs. A series of experiments using phantom and real MRIs was conducted and the results compared with those of the commonly used c-means (CM) method and dynamic contrast-enhanced (DCE) breast MRIs for performance evaluation. After comparison with the CM algorithm and DCE breast MRIs, the experimental results showed that the high-contrast images generated by the spectral signature detection technology, the KFLM, were of superior quality.

1. Introduction

Breast MRI involves the use of magnetic resonance imaging (MRI) to look specifically at the breast; it is a non-invasive procedure that doctors can use to determine what the inside of the breast looks like without having to perform surgery or flatten the breast (as in a mammogram). Each examination produces hundreds of images of the breast, cross-sectional in all three directions (side-to-side, top-to-bottom, and front-to-back), which are then read by a radiologist. No radioactivity is involved, and the technique is believed to pose no health hazards in general. The hope is that such non-invasive studies will contribute to our progress in learning how to predict the behavior of tumors and in selecting proper treatments [1].

The recent interest in MRI of the breast follows reports that malignant (or cancerous) lesions become brighter following a contrast agent injection. Contrast-enhanced breast magnetic resonance imaging has been shown to have a high sensitivity in the detection of breast cancer, particularly invasive breast cancers [2], and the accuracy is significantly higher than that of conventional imaging techniques (mammography and ultrasound) in the screening of high-risk women [3]. When performing MRI, three parameters, T1, T2, and PD, are usually applied to generate a multi-spectral image sequence that converts tissue variation into contrast in the images. For contrast enhancement, the breast is imaged several times in different sequences after the injection of a paramagnetic contrast agent, a so-called contrast injection. The screening is based on the hypothesis that after the injection of the agent, abnormalities are enhanced more than normal tissues due to their increased vascularity, vascular permeability and interstitial space [4]. Besides the discomfort of injection, the complexity of the contrast injection procedure is time-consuming and causes waste of medical resources.

Based on these considerations, this paper proposes an MRI classification and detection technology based on spectral feature correlation among breast MRI sequences, called the Kalman filter-based linear mixing method (KFLM) [5,6], for classifying breast MRIs into four high-contrast tissue-separated images. The KFLM applies the Kalman filter on the linear spectral mixture model of breast MRIs based on the assumption that breast MRIs contains multiple object signatures (i.e., fatty tissue, glandular tissue, tumor mass and muscle) with their complete knowledge; each MRI pixel is then regarded as a model construed by linear mixing of these object signatures [7–9]. The Kalman filter can reflect abrupt changes in signature abundance via an auxiliary equation called the abundance state equation (ASE), which traces, estimates and updates

* Corresponding author.
E-mail addresses: pcchung@ee.ncku.edu.tw, scyang@ncut.edu.tw (P.-C. Chung).

0895-6111/$ – see front matter © 2008 Elsevier Ltd. All rights reserved.
doi:10.1016/j.compmedimag.2008.12.001

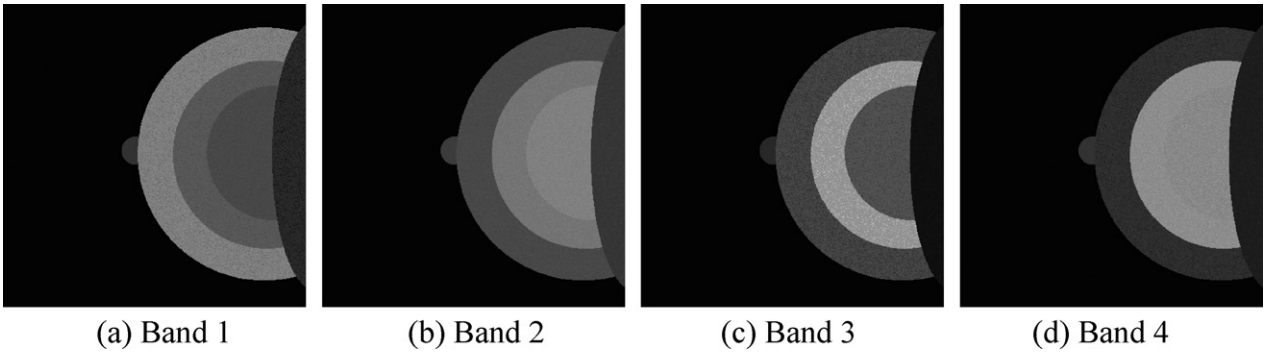

Fig. 1. Computer-simulated phantoms of the four bands.

Table 1
Average gray level values and variances used for the four bands of the computer-simulated phantoms in Fig. 1.

	MRI band	BK	Tissue							
			Fatty		Glandular		Tumor		Muscle	
			Average	Variance	Average	Variance	Average	Variance	Average	Variance
Band 1	3D Flash	3	125	101–138	87	71–92	72	67–78	38	14–47
Band 2	T1	3	72	66–78	116	110–126	128	119–135	54	50–64
Band 3	T2	3	65	40–78	151	140–206	78	50–85	15	9–18
Band 4	PD	3	45	31–54	141	130–152	136	124–151	29	26–40

the signature abundance recursively; it then estimates each of these substances by employing the abundance fractions of the substances as a base for classification. As a result, the gray scale of each pixel on the gray-scale image generated after the experiment represents the substance abundance fraction calculated using mixed-pixel classification.

One advantage of the Kalman filter-based linear mixing method over traditional classification techniques is the use of mixed-pixel classification, in which a linear spectral mixture model is used to describe the mixture of substances present in a pixel, rather than pure-pixel classification. Compared with mixed-pixel classification, pure-pixel classification can only achieve a binary decision to generate the binary (black and white) figure.

In order to validate our proposed system, computer-simulated phantoms were first used for quantitative analysis and evaluation of efficiency in a comparison of the KFLM approach and the CM method. Phantoms and real breast MRIs taken before and after contrast injection with four different parameters are also used to evaluate the feasibility of this technique in medical and clinical applications.

The organization of this paper is as follows. In Section 2, the classification of an MR image sequence as a linear mixing problem is formulated. The KFLM approach is described in Section 3, and the modified version of the CM method implemented in this study is discussed briefly in Section 4. Section 5 details a set of experiments conducted to evaluate the performance of the KFLM in MR classification, and also includes a comparison of the results of contrast-injected breast MRIs and those produced by the CM method. Concluding remarks are presented in Section 6.

2. Linear spectral mixture model

A breast MRI can be regarded as a three-dimensional image where the third dimension is a spectral dimension specified by TR/TE parameters, in which each pixel is actually a column vector and can be modeled by linear mixing. It is assumed that there are p spectrally distinct substances $\{\mathbf{m}_1, \mathbf{m}_2, \ldots, \mathbf{m}_p\}$ contained in the image, where $\mathbf{r}(x,y)$ describes the image pixel vector represented by a $l \times 1$ column vector and l is the number of spectral bands at position (x,y). Let $\mathbf{M}$ be a $l \times p$ signature matrix denoted by $[\mathbf{d}_1\mathbf{d}_2 \ldots \mathbf{d}_p]$,

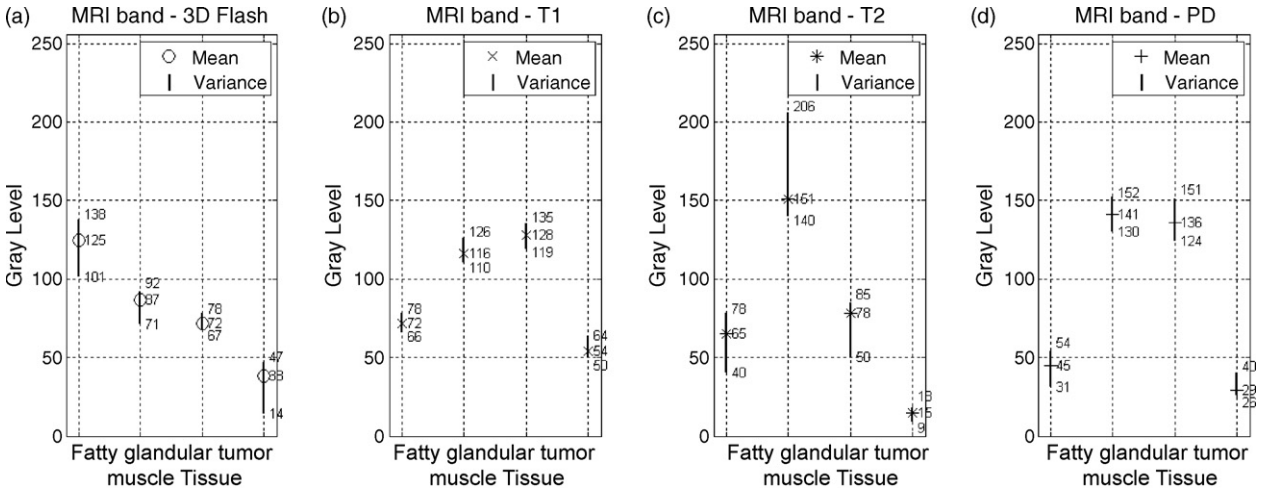

Fig. 2. Spectra distribution of the four computer-simulated phantoms shown in Fig. 1. (a) 3D Flash, (b) T1, (c) T2, and (d) PD.

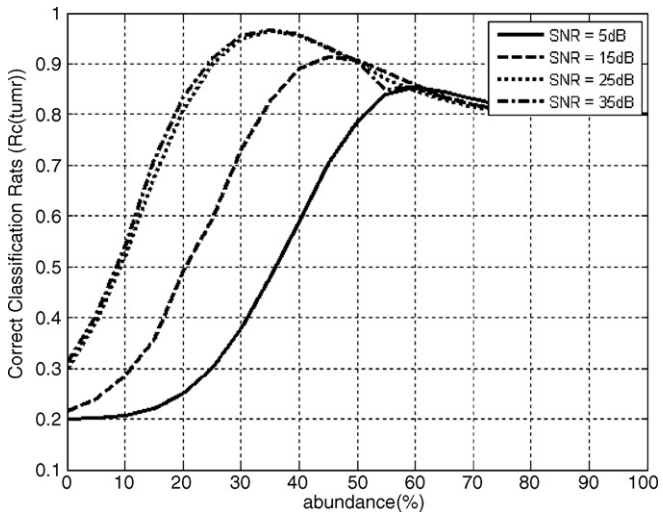

Fig. 3. Correct Classification Rats (Rc) curves of tumor classification in the KFLM for the cases of SNR = 5 dB, 15 dB, 25 dB and 35 dB, where the cutoff threshold value of *a*% was chosen to be 5%, 10%, 15%, 20%, 25%, 30%, 35%, 40%, 45%, 50%, 55%, 60%, 65%, 70%, 75%, 80%, 85%, 90%, 95% and 100%.

where $\boldsymbol{d}_j$ is a $l \times 1$ column vector representing the spectral signature of the jth substance $\mathbf{m}_j$ in pixel vector $\mathbf{r}$. It also assumed that $\boldsymbol{\alpha}(x,y)$ is a $p \times 1$ column vector associated with $\mathbf{M}$, which is defined as $\boldsymbol{\alpha} = (\alpha_1 \alpha_2 \ldots \alpha_p)^{\mathrm{T}}$, where α_j represents the value of $\mathbf{d}_j$, the jth signature in pixel vector $\mathbf{r}$. Lastly, $\mathbf{r}$ can be described as follows by the linear mixing model:

$$\boldsymbol{r}(x,y) = \boldsymbol{M}\boldsymbol{\alpha}(x,y) + \boldsymbol{n}(x,y) \tag{1}$$

where $\mathbf{n}$ is a $l \times 1$ column vector and is generated as additive noise or measurement error.

3. Kalman filter-based linear mixing method

The complete KFLM is composed of the linear mixing model of Eq. (1) and the abundance equation of the Kalman filter, as follows:

$$\boldsymbol{\alpha}(k+1) = \boldsymbol{\Phi}(k+1,k)\boldsymbol{\alpha}(k) + \boldsymbol{u}(k) \tag{2}$$

where k replaces the position (x,y) in Eq. (1), representing the discrete instant of time at which the pixel is processed. Vector $\boldsymbol{\alpha}(k)$ represents the value of abundance at time k, $\boldsymbol{\Phi}(k+1,k)$ is a known $p \times p$ state transition matrix that describes the change in abundance from time k to $k+1$, and, $\mathbf{u}(k)$ is a zero-mean $p \times 1$ abundance noise vector independent of $\boldsymbol{\alpha}(k)$, generated by the white process with a covariance matrix given by

$$E[\boldsymbol{u}(k)\mathbf{u}(m)^{\mathrm{T}}] = \boldsymbol{Q} = \sigma_2^2 \delta_{km} \boldsymbol{I}_{p\times p} \tag{3}$$

where σ_2^2 is the variance of the abundance noise vector, δ_{km} is Kronecker's notation, given by

$$\delta_{km} = \begin{cases} 1, & k = m \\ 0, & k \neq m \end{cases}$$

and matrix $\mathbf{I}_{p\times p}$ is a $p \times p$ identity matrix. Based on the discrete-time Kalman filtering notation at discrete time k, Eq. (1) is modified as

$$\boldsymbol{r}(k) = \boldsymbol{M}(k)\boldsymbol{\alpha}(k) + \boldsymbol{n}(k) \tag{4}$$

where vector $\mathbf{r}(k)$ is the observed pixel at time k, and $\mathbf{M}(k)$ is a known signature matrix at time k. The zero-mean measurement noise in Eq. (1) is represented as $\mathbf{n}(k)$, which is generated by the white process with a covariance matrix given by

$$E[\boldsymbol{n}(k)\boldsymbol{n}(m)^{\mathrm{T}}] = \boldsymbol{R} = \sigma_1^2 \boldsymbol{I}_{l\times l} \delta_{km} \tag{5}$$

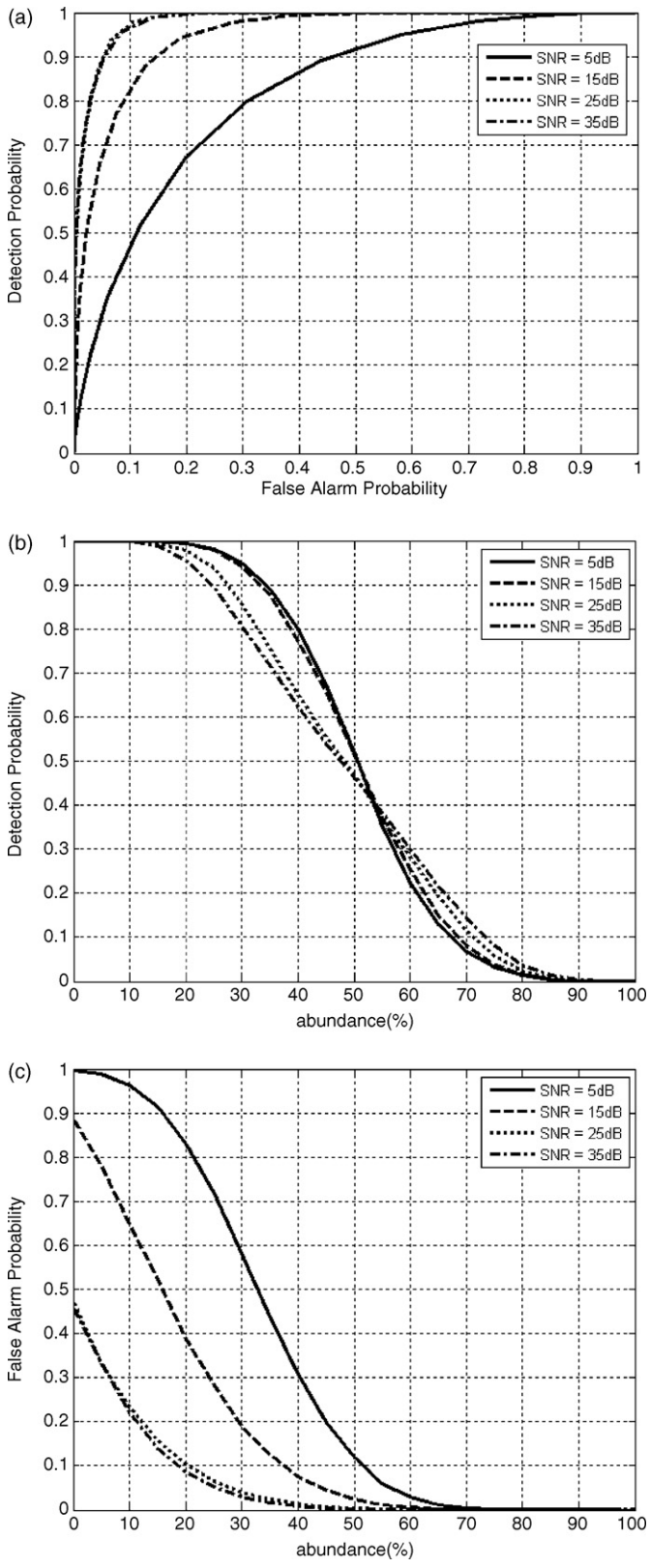

Fig. 4. Receiver operating characteristic (ROC) curves of the KFLM in computer-simulated phantoms (SNR = 5 dB, 15 dB, 25 dB and 35 dB). (a) R_D *vs.* R_F, (b) R_D *vs.* *a*%, and (c) R_F *vs.* *a*%.

Table 2
Correct Classification Rats (Rc) of the CM method and the KFLM for four target substances (a% of the KFLM is optimized).

		SNR = 5 dB	SNR = 15 dB	SNR = 25 dB	SNR = 35 dB
Fatty	CM	0.77137	0.91939	0.92063	0.93819
	KFLM	0.79547 (a% = 40%)	0.96335 (a% = 35%)	0.99873 (a% = 20%)	0.99676 (a% = 25%)
Glandular	CM	0.83247	0.90969	0.92735	0.93612
	KFLM	0.88155 (a% = 45%)	0.97646 (a% = 25%)	0.99858 (a% = 10%)	0.99091 (a% = 5%)
Muscle	CM	0.70090	0.78894	0.80671	0.83538
	KFLM	0.81370 (a% = 95%)	0.82916 (a% = 60%)	0.85880 (a% = 40%)	0.87636 (a% = 30%)
Tumor	CM	0.77339	0.83372	0.87645	0.92931
	KFLM	0.85399 (a% = 60%)	0.91465 (a% = 45%)	0.96473 (a% = 35%)	0.96691 (a% = 35%)

The purpose of the KFLM is to obtain the minimum mean-squared estimation of abundance state $\boldsymbol{\alpha}(k)$ with observed data $\mathbf{r}(k)$. Using knowledge of the predicted $\boldsymbol{\alpha}(k)$, we can classify and detect pixel $\mathbf{r}(k)$. Assuming $\widehat{\boldsymbol{\alpha}}(k+1|k)$ is the minimum mean-squared estimation of $\boldsymbol{\alpha}(k+1)$ obtained from the previously observed value $\mathbf{r}(j)$, with j from 1 to k, then $\widehat{\boldsymbol{\alpha}}(k|k)$ and $\widehat{\boldsymbol{\alpha}}(k|k-1)$ can be deduced by analogy. We further define $\mathbf{P}(k|k)$ as the error covariance matrix at time k from the previously observed $\mathbf{r}(j)$, with j from 1 to k, and $\mathbf{P}(k+1|k)$ as the prediction error covariance matrix at time $k+1$. Then, the KFLM is computed recursively to obtain the abundance vector of each pixel as the result of the classification. For more details on the implementation of the Kalman filter, refer to Ref. [6].

4. c-Means (CM) methods

In order to evaluate the performance of the KFLM approach, the widely used CM method [10] (also known as K-means in Ref. [11]) is used for comparative analysis. The reason for selecting the CM method for comparative purposes is twofold: first, it allows us to generate background signatures in an unsupervised manner for classification; second, it is basically a spatial-based pattern classification technique. As opposed to the KFLM approach, which only classifies objects of interest, the CM method classifies all MR image pixel vectors, including background pixel vectors, into pattern classes. In order to make a fair comparison, the CM method used here includes in its clustering procedure the same knowledge

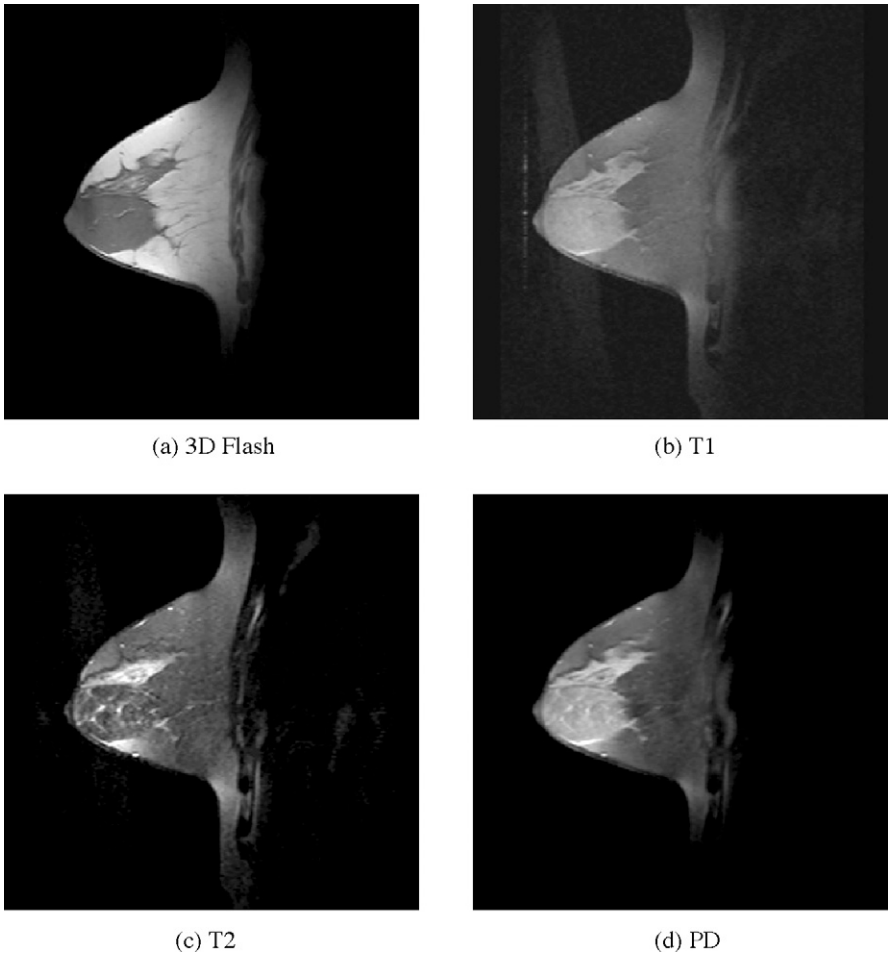

Fig. 5. Four bands of real breast MRIs. (a) Three-dimensional fast low-angle shot (3D Flash) gradient echo sequence (TR/TE = 12/5 ms, flip angle = 25°, matrix = 512 × 179), (b) sagittal image from fat-saturated T1-weighted turbo spin-echo (TR/TE = 832/20 ms, flip angle = 90°, matrix = 512 × 152), (c) T2-weighted fat-saturated image (TR/TE = 3000/105 ms, flip angle = 90°, matrix = 512 × 154), and (d) proton density fat-saturated image (TR/TE = 3000/15 ms, flip angle = 90°, matrix = 512 × 154).

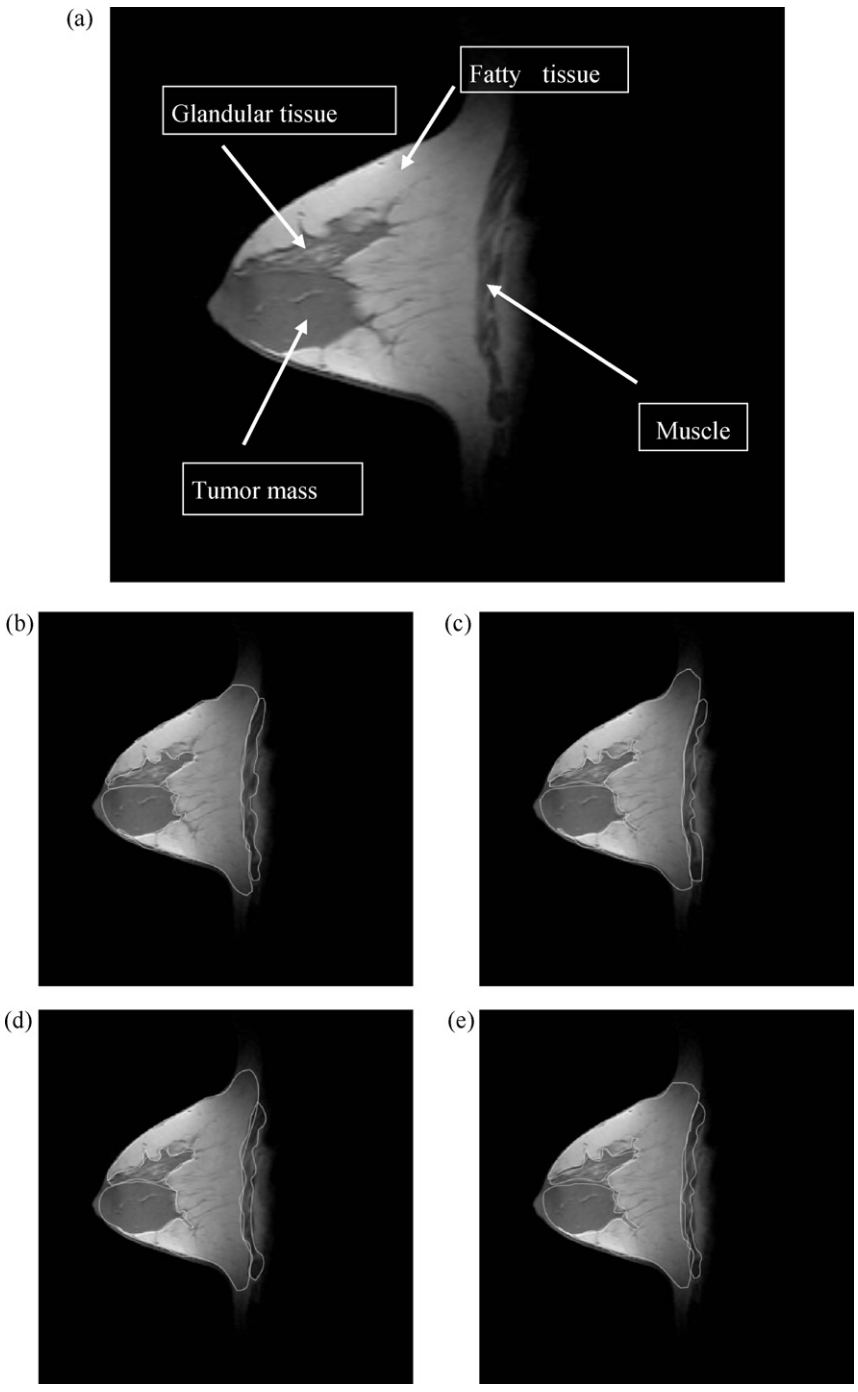

Fig. 6. (a) Four major tissues verified by experienced radiologists in real breast MRIs; (b)–(d) the contours of the four major tissues as delineated by three different experienced radiologists; (e) the result of the intersection of (b)–(d).

of objects of interest that is required by the KFLM approach. The CM method implemented in this paper for experiments is a modified version of the commonly used CM method, which is also referred to as ISODATA in Refs. [10,11].

Let the spectral signatures of p objects of interest be denoted by $\{\boldsymbol{d}_i\}_{i=1}^{p}$, where $\mathbf{d}_i$ is the spectral signature of the ith object. The implementation of the CM method is described in detail below.

4.1. CM method

(1) Determine the number of pattern classes, $c \geq p$, and let $\{\boldsymbol{\mu}_i\}_{i=1}^{c}$ be their corresponding class means.

(2) Initialization:

Let $k = 0$ and the p class means not be fixed at $\boldsymbol{\mu}_i^{(0)} = \boldsymbol{d}_i$. All class means $\boldsymbol{\mu}_i^{(0)}$, $i > p$ are selected. $\{d_i\}_{i=1}^{p}$ must be in a different class.

(3) At the kth iteration, compute the distance of each sample pixel vector from all class means, $\boldsymbol{\mu}_i^{(k)}$ for $1 \leq i \leq c$ and assign the sample vector to the class whose mean is the shortest distance from the sample vector.

(4) For each class i with $p \leq i \leq c$, recompute the class mean by averaging the sample vectors in the class, denoted by $\hat{\boldsymbol{\mu}}_i^{(k)}$. Let $k \leftarrow k+1$, $\boldsymbol{\mu}_i^{(k)} = \mathbf{d}_i$, $1 \leq i \leq p$ and $\boldsymbol{\mu}_i^{(k)} \leftarrow \hat{\boldsymbol{\mu}}_i^{(k)}$ for $p \leq i \leq c$.

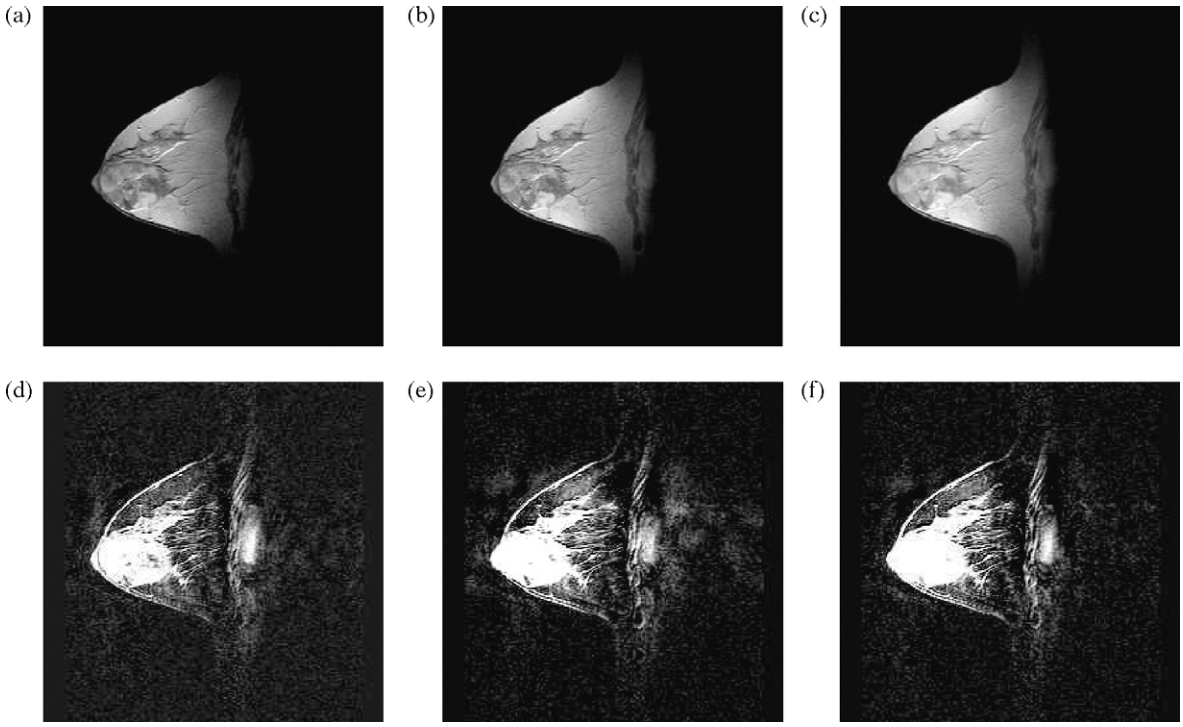

Fig. 7. Real breast MRIs acquired by contrast injection: (a)–(c) are 3D Flash contrast-enhanced images obtained 1 min, 3 min and 5 min after intravenous administration of a contrast agent, respectively; (d)–(f) are dynamic contrast-enhanced breast MRIs with subtraction, the subtracted image obtained 1 min, 3 min and 5 min after intravenous administration of the contrast agent, respectively, from the image taken before contrast agent injection.

(5) If any class mean changes in the set $\{\boldsymbol{\mu}_i^{(k)}\}_{i=p}^{c}$, go to step 3.

It should be noted that knowledge of $\{\boldsymbol{d}_i\}_{i=1}^{p}$ is required *a priori*. Therefore, the first p class means are fixed during iteration; however, the class means, $\{\boldsymbol{\mu}_i^{(k)}\}_{i=p}^{c}$, are regenerated at each iteration by the CM method in a supervised manner using the minimum distance as a criterion. These generated class means are considered to be signatures of unknown signal sources, which are not provided by prior knowledge and may include background signatures.

5. Experimental results

This section describes a series of experiments based on computer-simulated phantoms and real breast MRIs. Use of computer-simulated phantoms allows us to carry out quantitative research and error analysis on the FKLM, while real breast MRIs are used to evaluate the effectiveness and practicality of the KFLM in medical clinical diagnosis.

5.1. Computer-simulated phantoms evaluation

In this section, we utilize a series of computer-simulated phantoms for quantitative analysis, efficiency evaluation and performance comparison between the KFLM approach and the CM method. The number of classes in the CM method is set at 5, representing the five classes of major tissues, which are fatty tissue, glandular tissue, tumor, muscle and background, in breast MRI. The phantoms generated by the computer in four difference bands are shown in Fig. 1, at 419×419 in size. The four semicircles represent four areas of breast tissue, which from left to right are nipple, fatty tissue, glandular tissue and tumor, while the semi-ellipse in the rightmost represents an area of muscle. For a better reflection of the characteristics of real breast MRIs, the gray level values in the tissue area in each band of the computer-simulated phantoms correspond to the average and variance of each tissue area in real breast MRIs, which were verified by three experienced radiologists, as shown in Fig. 6(e).

Table 1 tabulates the names of the parameters used in the MRI pulse sequence and the average gray level values and variance for the tissues in each band. Due to the fact that noise may be caused by the magnetic field of static, radio frequency and gradient or other factors during acquisition of the MRI, zero-mean Gaussian noise was added to the phantom images in Fig. 1 so as to achieve different levels of signal-to-noise ratio (SNR), ranging from 5 dB to 35 dB. These phantoms with different levels of signal-to-noise ratio also serve to illustrate the proposed KFLM technique and demonstrate its advantages.

5.1.1. Abundance percentage thresholding method

In the application of the KFLM approach to these simulated images, the signature matrix $\mathbf{M}$ is assigned four objects of interest, which are fatty tissue, glandular tissue, tumor and muscle, as shown in Fig. 2. As mentioned above, the images generated by the KFLM have gray level values that are in proportion to the detected abundance fraction of $\mathbf{M}$. On the other hand, the CM method is a classical class-labeling process in which each data sample vector is assigned to only one class. Therefore, images generated by the CM method are classification images, rather than gray-scale images as are generated by the KFLM approach. To carry out the quantitative study and compare the results with those of the CM method, we converted the abundance fractional images generated by the KFLM to binary images; thus, we adopted the method proposed in Ref. [12], which uses the abundance fraction percentage as the cut-off threshold value for such a conversion. We first normalized the abundance fraction of the image with the range of [0,1]. More specifically, let $\mathbf{r}$ be the pixel vector of the image and $\hat{\alpha}_1(r), \hat{\alpha}_2(r), \cdots, \hat{\alpha}_p(r)$ be the estimated abundance fractions of $\alpha_1, \alpha_2, \ldots, \alpha_p$ in $\mathbf{r}$; then the normalized abundance fraction, $\widetilde{\alpha}_j(\mathbf{r})$, of each estimated abundance

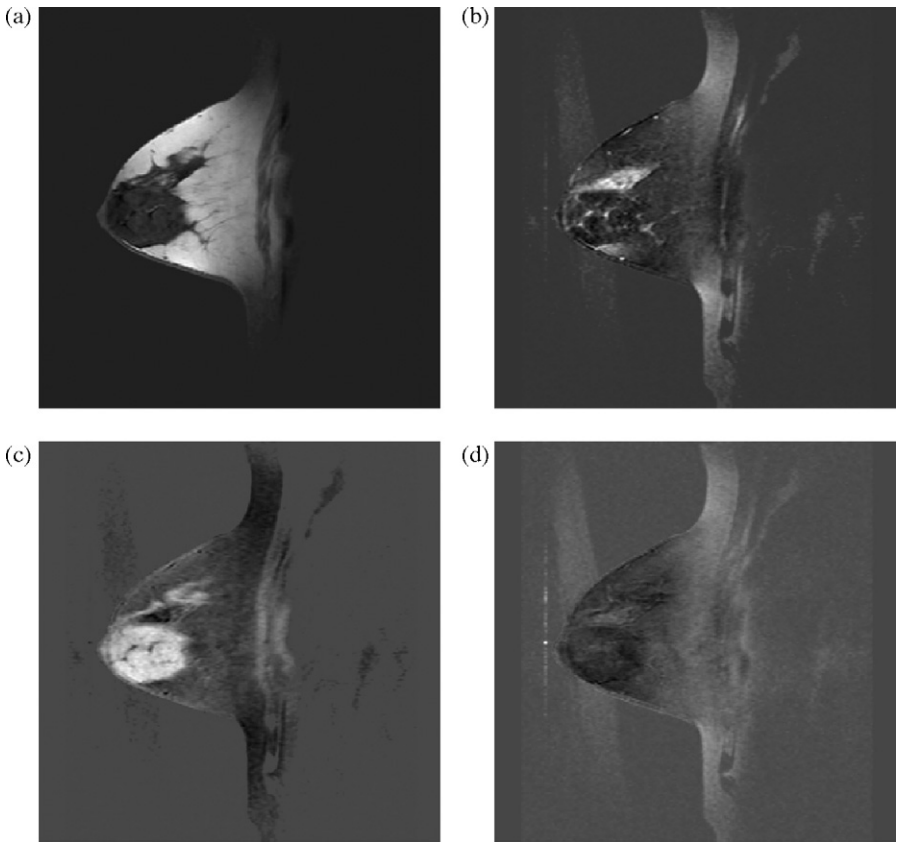

Fig. 8. High-contrast images acquired by the proposed KFLM method: (a) fatty tissue, (b) glandular tissue, (c) tumor, and (d) muscle.

fraction $\hat{\alpha}_j(\mathbf{r})$ can be obtained by

$$\widetilde{\alpha}_j(\mathbf{r}) = \frac{\hat{\alpha}_j(\mathbf{r}) - \min_{\mathbf{r}}\hat{\alpha}_j(\mathbf{r})}{\max_{\mathbf{r}}\hat{\alpha}_j(\mathbf{r}) - \min_{\mathbf{r}}\hat{\alpha}_j(\mathbf{r})} \tag{6}$$

Assume that $a\%$ is the cutoff abundance fraction threshold value; i.e., if the normalized abundance fraction of the pixel vector is greater than or equal to $a\%$, then the pixel will be detected as a desired object pixel and set to "1"; otherwise, it will be set to "0", meaning it is not detected as a desired object pixel. In the sequel, the use of this cutoff threshold value to threshold a fractional abundance image will be referred to as the $a\%$ thresholding method. Fig. 3 shows the Correct Classification Rats (Rc) curves of tumor classification in the KFLM for the case of SNR = 5 dB, 15 dB, 25 dB and 35 dB, where the cutoff threshold value of $a\%$ was chosen to be 5%, 10%, 15%, 20%, 25%, 30%, 35%, 40%, 45%, 50%, 55%, 60%, 65%, 70%, 75%, 80%, 85%, 90%, 95% and 100% and the Correct Classification Rats (Rc) was as defined in Eq. (11). From Fig. 3, it can be seen that the system has an optimal Rc when $a\%$ = 35% for both SNR = 25 dB and 35 dB, $a\%$ = 45% for SNR = 15 dB, and $a\%$ = 60% for SNR = 5 dB.

5.1.2. Receiver operating characteristic (ROC) curve analysis

Using the abovementioned $a\%$ thresholding method, we were able to calculate the number of detected pixels in the generated fractional abundance image. This subsection further utilizes the ROC curve for analysis based on the gradually increasing $a\%$. First, let $\{\boldsymbol{d}_i\}_{i=1}^{p}$ be a set of objects of interest for classification; then, we define $N(\mathbf{d}_i)$ as the total number of pixels specified by the ith object signature $\mathbf{d}_i$, $N_D(\mathbf{d}_i)$ as the number of pixels specified by the i-th object signature $\mathbf{d}_i$ and actually detected as the $\mathbf{d}_i$, and $N_F(\mathbf{d}_i)$ as the number of false alarm pixels that are not specified by the object signature $\mathbf{d}_i$ but are detected as $\mathbf{d}_i$. Using the definitions of $N(\mathbf{d}_i)$, $N_D(\mathbf{d}_i)$ and $N_F(\mathbf{d}_i)$, we further define the detection rate $R_D(\mathbf{d}_i)$ and the false alarm rate $R_F(\mathbf{d}_i)$ for a particular object signature $\mathbf{d}_i$ by

$$R_D(\boldsymbol{d}_i) = \frac{N_D(\boldsymbol{d}_i)}{N(\boldsymbol{d}_i)} \tag{7}$$

$$R_F(\boldsymbol{d}_i) = \frac{N_F(\boldsymbol{d}_i)}{N - N(\boldsymbol{d}_i)} \tag{8}$$

and the mean detection rate R_D and mean false alarm rate R_F for all object signatures by

$$R_D = \sum_{i=1}^{p} R_D(\boldsymbol{d}_i)p(\boldsymbol{d}_i) \tag{9}$$

$$R_F = \sum_{i=1}^{p} R_F(\boldsymbol{d}_i)p(\boldsymbol{d}_i) \tag{10}$$

where N is the total number of pixels in the image and $p(\boldsymbol{d}_i) = N(\boldsymbol{d}_i)/\sum_{i=1}^{p} N(\mathrm{d}_i)$. Note that the mean detection rate R_D as defined by Eq. (9) is the average of the detection rates for all detected objects; similarly, the mean false alarm rate R_F as defined by Eq. (10) is the average of the false alarm rates for all detected objects. According to Eqs. (7)–(10), each fixed $a\%$ can generate a pair of R_D and R_F. Furthermore, increasing $a\%$ from 0% to 100% gradually can generate a set of pairs (R_D, R_F). In this experiment, we adopted the method proposed in Refs. [13,14] of plotting the ROC curves of (R_D, R_F), $(R_D, a\%)$ and $(R_F, a\%)$. Fig. 4(a)–(c) shows the ROC curves of (R_D, R_F), $(R_D, a\%)$ and $(R_F, a\%)$, respectively, for SNR = 5 dB, 15 dB, 25 dB and 35 dB. The 2D curves of (R_D, R_F) in Fig. 4(a) provide the mean detection rate *vs.* the mean false alarm rate of the classifier. As seen in Fig. 4(a), the performance of the KFLM is excellent when SNR = 25 dB and 35 dB, and degrades when SNR is decreased. Moreover, the ROC curves of $(R_D, a\%)$ and $(R_F, a\%)$ in Fig. 4(b) and (c) indicate how the threshold $a\%$ affects the efficiency of the classifier. Fig. 4(b) shows the efficiency of the KFLM with four different SNRs: similarly, the R_D began to drop gradually from $a\%$ = 20%, then rapidly

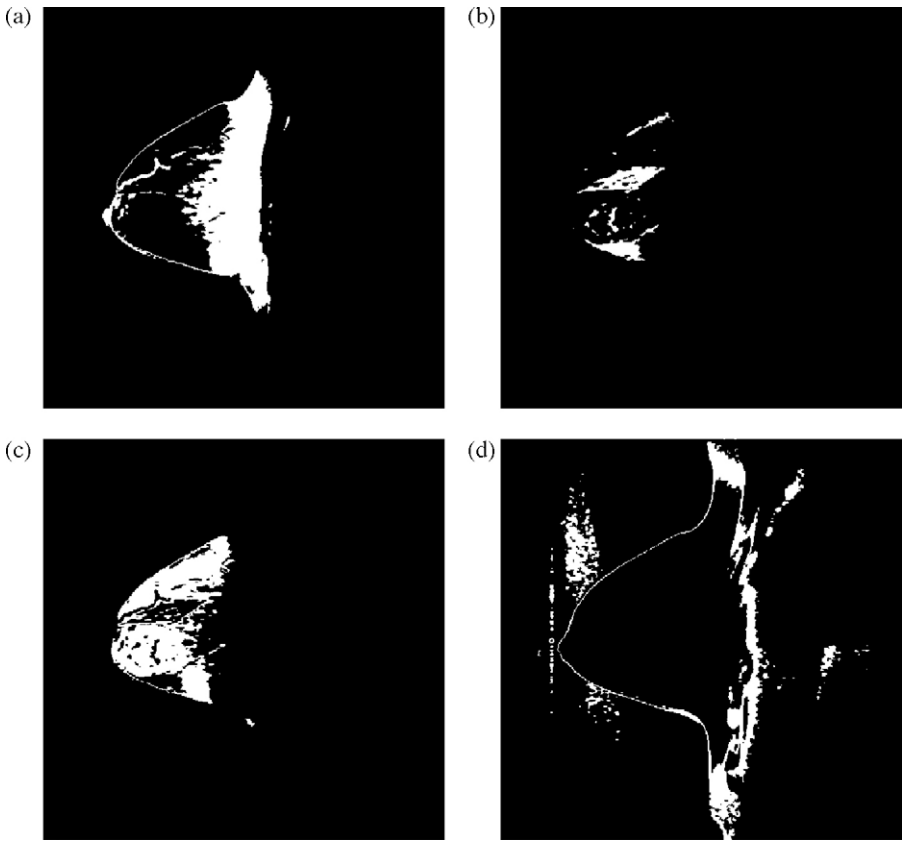

Fig. 9. Four major tissue classification results using the traditional method, CM: (a) fatty tissue, (b) glandular tissue, (c) tumor, and (d) muscle.

between 30% and 70%, and finally closed to zero after 80%. Fig. 4(c) also exhibits results that were similar but more distinct among the four different SNRs, and clearly indicates that when SNR = 25 dB and 35 dB, the R_F of the KFLM drops rapidly between $a\% = 0\%$ and 30%, and reaches zero around $a\% = 40\%$; the R_F of the KFLM with SNR = 5 dB also drops rapidly from $a\% = 15$–55% and reaches zero around $a\% = 60\%$. When the SNR is 15 dB, the R_F of the KFLM curves are approximately between the curves of 5 dB and 25 dB. From Fig. 4(b) and (c), we can see that a good compromise of $a\%$ for SNR = 25 dB and 35 dB between R_D and R_F is around 25%, 35% for SNR = 15 dB, and 45% for SNR = 5 dB.

To compare the classification performance of the KFLM with that of the CM method, we further define the Correct Classification Rats (Rc) for a particular object signature as follows:

$$\mathrm{Rc} = \frac{N_D(\boldsymbol{d}_i) + N_N(\boldsymbol{d}_i)}{N} \tag{11}$$

where $N_N(\mathbf{d}_i)$ represents the number of pixels that are not specified by the ith object signature $\mathbf{d}_i$ and classified into non-object pixels accurately. Table 2 tabulates the calculated R_c of the KFLM and the CM method with different objects and SNRs, from which we can see that the KFLM performs better than the CM method with an appropriate choice of $a\%$, especially for high-noise images, which conforms to the characteristics of breast MRIs.

5.2. Real MRI experiments

In the following experiments, real breast MRIs acquired from patients with abnormal pathologies were used for performance evaluation. MRIs were performed on a 1.5-T Magnetum Vision plus system (Siemens, Erlangen, Germany). One sagittal section of the images is shown in Fig. 5(a)–(d), with the four different bands corresponding to the parameters given in Table 1, in which band 1 is the dynamic contrast-enhanced (DCE) three-dimensional fast low-angle shot (3D Flash) gradient echo sequence acquired with TR/TE (repetition time/echo time) = 12/5 ms, band 2 is the T1-weighted spin-echo image acquired with TR/TE = 832/20 ms, band 3 is the fat-saturated T2-weighted spin-echo image acquired with TR/TE = 3000/105 ms, and band 4 is the PD-weighted spectral image acquired with TR/TE = 3000/15 ms. The slice thickness of all MRIs was 3 mm. In many breast MRI applications, fatty tissue, glandular tissue, tumor and muscle are the tissues of major interest, and knowledge of these tissues can generally be obtained directly from the images. In our experiments, the spectral signatures of the four major interest tissues required for the KFLM approach were extracted directly from breast MRIs and verified by experienced radiologists, the results of which are shown in Fig. 6(a), and Fig. 6(b)–(d) shows the contours of the four major tissues delineated by three different experienced radiologists. Fig. 6(e) is the result of the intersection of Fig. 6(b)–(d), which was used for sampling the average gray level values and the variance of the tissues in each band for the computer-simulated phantoms in previous subsection, and is also used as the ground truth for tissue classification evaluation.

It is worth to be noted that dynamic contrast-enhanced MR imaging has emerged as a very promising modality for the detection and diagnosis of breast cancer. While conventional mammography and breast ultrasonography demonstrate morphologic changes in breast tumor, DCE MR imaging depict malignant findings by showing the pathologic vascularization of the breast cancer. However, the enhancement patterns of gadolinium-enhanced benign and malignant lesions have been reported to overlap in several series, the specificity and tissue characterization of MR imaging continues to be problematic. Limitations of breast MR imaging include low specificity (varied from 37% to 97%) and relative low sensitivity in the detection of ductal carcinoma in situ (DCIS). The main

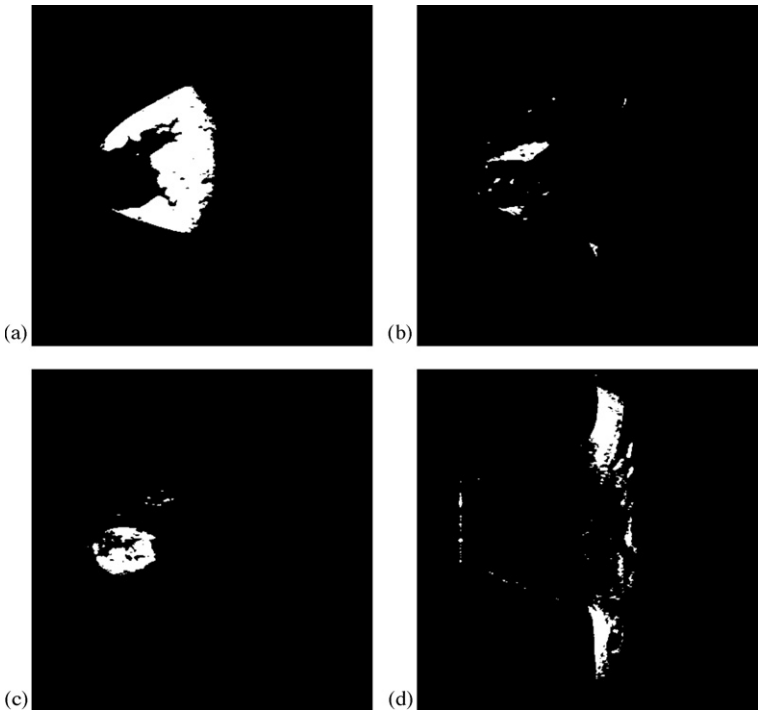

Fig. 10. Four major tissue classification results using the proposed method, the KFLM, with the best cutoff threshold: (a) fatty tissue, (b) glandular tissue, (c) tumor, and (d) muscle.

advantage of DCE MR imaging is its high sensitivity (range from 94% to 99%) for invasive breast cancer. Since dynamic contrast enhancement is routine imaging sequence on breast MR examination, the DCE breast MRIs were conducted for comparison with the images generated by proposed method. Fig. 7(a)–(c) shows dynamic contrast-enhanced breast MRIs imaged at different lengths of time after traditional contrast injection, and Fig. 7(d)–(f) shows dynamic contrast-enhanced breast MRIs with subtraction, acquired by subtraction of the images before and after the injection of contrast material. Fig. 8(a)–(d) shows the high-contrast images resulting from using the proposed KFLM approach in Fig. 5(a)–(d). It can be seen that the object tissues in the images generated by the KFLM are of greater contrast and accuracy than those imaged by contrast injection. Moreover, glandular tissue and tumor tissue are successfully demarcated in Fig. 8(c) but not in Fig. 7(a)–(f).

Fig. 9(a)–(d) shows the results of applying the traditional CM method on the images shown in Fig. 5(a)–(d), in which fatty tissue, glandular tissue, tumor and muscle are shown in (a), (b), (c) and (d), respectively. As we can see, the CM method does not perform as well as does the KFLM method due to the fact that it is a pure-pixel and spatial analysis-based pattern classification technique. In addition, Fig. 10(a)–(d) shows the results of applying the proposed KFLM method on the images in Fig. 5(a)–(d) using the best cutoff threshold: fatty tissue, glandular tissue, tumor and muscle are shown in (a), (b), (c) and (d), respectively. Comparing Figs. 9 and 10 with Fig. 6(e), we find that the object area classified by the proposed KFLM approach is more accurate than that identified by the traditional CM method. These results coincide with the results of the evaluation using computer-simulated phantoms.

6. Conclusion

This paper proposed a spectral signature detection technology based on spectral analysis for the generation of contrast enhancement images and classification of the major tissues in breast MRI, called the Kalman filter-based linear mixing method. It is assumed that breast MRIs contain multiple object signatures (i.e., fatty tissue, glandular tissue, tumor mass, and muscle) with their complete knowledge and each pixel in the image is then regarded as a model construed by linear mixing of those object signatures. In classical spatial-based pattern classification, the data must be classified into a number of pattern classes, and algorithms based on shape and feature analysis are unreliable due to the changeability of the soft tissues. The KFLM approach proposed by this paper remedies these flaws by utilizing an abundance state equation in the linear mixture model, so that the change in the signature abundance from pixel to pixel can be detected. Finally, using the KFLM approach the particular object signature can be extracted from the linear mixture model.

The experimental results indicate the promising possibilities of this proposed approach. Compared with the commonly used spatial-based pattern classification method, CM, and dynamic contrast-enhanced breast MRIs, the KFLM approach has been proven to be of better quality, able to correctly classify breast MRIs into four high-contrast tissue-separated images. We anticipate that these high-contrast images will assist radiologists and improve accuracy in breast tumor screening.

References

[1] http://www.mrsc.ucsf.edu/breast/.
[2] American College of Radiology. Breast imaging reporting and data system- magnetic resonance imaging, 1st ed. Reston, Va: American College of Radiology, 2003.
[3] Kuhl CK, Schmutzler RK, Leutner CC, Kempe A, Wardelmann E, Hocke A, et al. Breast MR imaging screening in 192 women proved or suspected to be carriers of a breast cancer susceptibility gene: preliminary results 1. Radiology 2000;215:267–79.
[4] Heywang-Kobrunner S, Beck R. Contrast-enhanced MRI of the breast. 2nd edition Springer-Verlag; 1996.
[5] Chang C-I, Brumbley C. A Kalman filtering approach to multispectral image classification and detection of changes in signature abundance. IEEE Trans Geosci Remote Sens 1999;37(January):257–68.
[6] Haykin S. Adaptive filtering theory. 3rd edition Englewood Cliffs, NJ: Prentice-Hall; 1996.
[7] Wang CM, Chen CC, Chung YN, Yang SC. Detection of spectral signatures in multispectral MR images for classification. IEEE Trans Med Imag 2003;12(1 (January)):50–61.

[8] Wang CM, Chen CC, Yang SC. An unsupervised orthogonal subspace projection approach to MR image classification. Opt Eng 2002;41(July):1546–57.
[9] Wang CM, Yang SC. Orthogonal subspace projection-base approaches to classification of MR images sequences. Comput Med Imag Graph 2001;25(6 (December)):465–76.
[10] Schalkoff R. Pattern recognition: statistical, structural and neural approaches. New York: Wiley; 1992.
[11] Duda RO, Hart PE. Pattern classification and scene analysis. New York: Wiley; 1973.
[12] Chang C-I, Ren H. An experiment-based quantitative and comparative analysis of hyperspectral target detection and image classification algorithms. IEEE Trans Geosci Remote Sens 2000;38(March):1044–63.
[13] Chang C-I, Ren H, Du Q, Chiang S-S, Ifarraguerri A. An ROC analysis for subpixel detection. In: Presented at the IEEE 2001 International Geoscience and Remote Sensing Symposium. 2001.
[14] Metz CE. ROC methodology in radiological imaging. Invest Radiol 1986;21: 720–3.

Sheng-Chih Yang received his M.S. degree in Computer and Information Science from Knowledge System Institute, IL, USA. in 1996 and Ph.D. degree in Electrical Engineering from National Cheng-Kung University, Tainan, Taiwan, ROC, in 2006. From 1996 to 2005, he worked as a lecturer at the Department of Electronic Engineering, National Chin-Yi University of Technology, and is an associate professor at the Department of Computer Science and Information Engineering, since 2006. His research interests include image processing and biomedical image processing.

Chuin-Mu Wang received his B.S. degree in Electronic Engineering from National Taipei Institute of Technology and his M.S. degree in Information Engineering from Tatung University of Taiwan in 1984 and 1990, respectively, and the Ph.D. degree in Electrical Engineering from National Cheng-Kung University, Taiwan, ROC, in 2002. Form 1984 to 1990, he was a system programmer on an IBM mainframe system and form 1990 to 1992 he was a marketing engineer on computer products at Tatung Company. Since 2002, he has been an associate professor at the National Chin-Yi University of Technology. His research interests include image processing, multispectral image processing, and medical imaging.

Hsian-He Hsu received his M.D. degree from National Defense Medical Center, Taiwan, in 1989. He is currently an attending Radiologist at Tri-Service General Hospital, National Defense Medical Center, Taiwan, ROC. His research interests include X-ray mammograms, ultrasound screening of breast cancer, computed tomography, and magnetic resonance imaging.

Pau-Choo (Julia) Chung received the B.S. and M.S. degrees in Electrical Engineering from National Cheng Kung University, Taiwan, ROC, in 1981 and 1983, respectively, and the Ph.D. degree in Electrical Engineering from Texas Tech University in 1991. She then joined the Department of Electrical Engineering, National Cheng Kung University, Taiwan, and has become a full professor since 1996. Since 2001, she has served as the Vice Director, and currently the Director, of the Center for Research of E-life Digital Technology, National Cheng Kung University. She was selected as Distinguished Professor of National Cheng Kung University in 2005. She also served as the Director of Electrical Laboratory, National Cheng Kung University, during 2005–2008.Dr. Chung's research interests include image analysis and pattern recognition, video image analysis, neural networks, telemedicine, and multimedia processing. Particularly she applies most of her research results on medical applications and received many awards. Dr. Chung has served as the program committee member in many international conferences. She is currently the chair of the IEEE Life Science Systems and Applications Technical Committee. She is also a member of the IEEE Visual Signal Processing and Communication Technical Committee, the IEEE Neural Systems and Applications Technical Committee, and the Multimedia Systems & Applications Technical Committee in the CASS. Currently she is also serving as the Associate Editor of Journal of Information Science and Engineering, the Guest Editor of IEEE Transactions on Circuits and Systems-I, a Member on IEEE International Steering Committee, IEEE Asian Pacific Conference on Circuits and Systems. She was the Chair of IEEE Computational Intelligence Society, Tainan Chapter (2005–2006), the Secretary General of Biomedical Engineering Society of the Republic of China (2005–2006), and Delegate in International Federation for Medical and Biological Engineering (IFMBE). She is one of the co-founders of Medical Image Standard Association at Taiwan. She is currently a member in BoG of CAS Society (2007–2009).She is a member of Phi Tau Phi honor society and IEEE Fellow.

Giu-Cheng Hsu received his M.D. degree from National Defense Medical Center, Taiwan, in 1984. He is currently an attending radiologist and an assistant professor at Tri-Service General Hospital, National Defense Medical Center, Taiwan, ROC. His fields of research include screening and diagnosis of breast cancer with mammography, ultrasound and magnetic resonance imaging.

Chun-Jung Juan has received his M.D. degree from National Defense Medical Center in 1995 and Ph.D. degree in the field of Electrical Engineering from National Taiwan University in 2007, in Taiwan. He is currently an assistant professor in the Department of Radiology at National Defense Medical Center and an attending Radiologist at Tri-Service General Hospital, Taiwan, ROC. His research interests focus on qualitative and quantitative investigation of biomedical imaging including computed tomography and magnetic resonance imaging.

Chien-Shun Lo received the B.S. and M.S. degree in Information Engineering and Computer Science from Feng-Chia University, Taiwan, ROC, in 1992 and 1994, respectively, and the Ph.D. degree in Electrical Engineering from National Cheng-Kung University, Taiwan, ROC, in 2000. From 2000 to 2004, he was with Newsoft Technology Corporation working on the development of multimedia and MPEG technology. Since October 2004, he has been with Department of Multimedia Design, National Formosa University, where he is currently an Assistant Professor. His current research includes computer aided diagnostic system design, medical image processing, video processing, and streaming technology.